Received: 6 September 2020 | Revised: 8 October 2020 | Accepted: 12 October 2020

DOI: 10.1111/ffe.13372

ORIGINAL CONTRIBUTION

FFEMS Fatigue & Fracture of Engineering Materials & Structures WILEY

Enhancing ductility and fatigue strength of additively manufactured metallic materials by preheating the build platform

P.D. Nezhadfar[1,2] | **Nima Shamsaei**[1,2] | **Nam Phan**[3]

[1]Department of Mechanical Engineering, Auburn University, Auburn, AL, 36849, USA

[2]National Center for Additive Manufacturing Excellence (NCAME), Auburn University, Auburn, AL, 36849, USA

[3]Structures Division, Naval Air Systems Command (NAVAIR), Patuxent River, MD, 20670, USA

Correspondence
Nima Shamsaei, National Center for Additive Manufacturing Excellence (NCAME), Auburn University, Auburn, AL 36849, USA.
Email: shamsaei@auburn.edu

Funding information
U.S. Naval Air Systems Command (NAVAIR)

Abstract

The effect of preheating the build platform (process) on the microstructure/defect structure (structure) as well as the tensile and fatigue behaviour (property) of the laser beam powder bed fused (LB-PBF) 316L stainless steel (SS) is investigated. Preheating the build platform to 150°C (P150) affects the thermal gradient and cooling rate resulting in the reduction of the volumetric defects (i.e., gas-entrapped pores and lack of fusion (LoF)) as compared with the condition where the build platform is non-preheated (NP). The ductility of P150 LB-PBF 316L SS is improved as compared with the NP counterpart, resulting from the less volumetric defects as well as the change in the crystallographic orientation of the grains in P150 condition. In addition, preheating the build platform is found to enhance the fatigue resistance of LB-PBF 316L SS specimens. This is associated with fewer and smaller volumetric defects in P150 specimens as compared with the NP ones.

KEYWORDS

laser beam powder bed fusion (LB-PBF), mechanical properties, microstructure, porosity, preheating, stainless steel

1 | INTRODUCTION

Additive manufacturing (AM) is an intricate metallurgical process comprising rapid melting and solidification regimes, which can be beneficial or detrimental to the mechanical performance of the material. The high cooling/solidification rate of the AM process typically leads to a relatively fine microstructure, which enhances the static strength of AM materials, in most cases superior to that of the wrought counterparts.[1] However, such cooling/solidification rates may also lead to the formation of volumetric defects (e.g., gas-entrapped pores and lack of fusion (LoF)), residual stresses and heterogeneous anisotropic microstructures, which can be detrimental to the fatigue resistance of the material.[2] Qualifying AM materials for the load-bearing applications prone to cyclic loading is known to be one of the main challenges for adoption of AM technology by several key industries.[3] Solberg and Berto[4] have recently overviewed and compared the fatigue performance of different AM materials such as Inconel 718, Ti-6Al-4V and several stainless steels (SS) with that of their wrought counterparts. They reported that in most cases for AM materials with the machined surface condition, the fatigue performance is deteriorated due to the presence of the volumetric defects formed during the AM processes.

Formation of the volumetric defects (i.e., gas-entrapped pores, LoF) in the AM materials is associated

with the thermal history experienced by the part throughout the fabrication process.[5–7] Variation in the thermal history can be related to the part size and geometry,[8,9] interlayer time interval,[10] the building environment (i.e., shielding gas type)[11] and process parameters (e.g., laser power and scan strategy).[12] In fact, the solidification rate (R), temperature gradient (G) and consequently the cooling rate ($R \times G$) are influenced by the aforementioned factors, which may alter the final structure (i.e., grain structure, level of defects and surface roughness) within the AM material.[5,13–15] For instance, if the part is large or the interlayer time interval is short, more heat accumulates in the part and reduces the cooling rate, and as a result, a more homogenized microstructure with less volumetric defects will be produced.[9,10] Furthermore, optimizing the process parameters (i.e., laser power, scan speed and scan strategy) to obtain higher heat input to the material, and therefore, lower cooling rate and temperature gradient, may result into proper melt pool overlap, which reduces the level of LoF defects in the AM material.[6,16] However, excessive heat input may result in the formation of keyhole defects; therefore, process parameters windows are to be developed for different materials/parts and AM systems.[17]

Altering the thermal history that a part experiences during the AM process, however, is not limited to the above-mentioned factors (i.e., part size geometry, interlayer time interval, laser power and scan speed). It has been shown that preheating the build platform can also play an important role in the final structure and reducing the anisotropy in tensile behaviour of the AM materials.[18] Yang et al.[19] reported that the size and volume fraction of equiaxed grains in laser beam powder bed fused (LB-PBF) Al-Mg(-Sc)-Zr are sensitive to the energy density applied and the build platform temperature. They showed that columnar grains transform to the equiaxed grains by increasing the energy density via decreasing the scan speed and preheating the build platform up to 200°C. This was attributed to the influence of lower thermal gradients as well as increased remelting zone volumes (i.e., larger melt pools). Preheating the build platform was also shown to be effective in altering the microstructure of an electron beam powder bed fused (EB-PBF) Inconel 718.[20]

Although the effect of preheating the build platform on the residual stresses and final grain structure has been investigated to some extent,[18,21,22] the effect of preheating on the fatigue performance of AM parts is not yet studied to the best of our knowledge. Therefore, the goal of this study is to evaluate the effect of build platform preheating not only on the microstructure/defect structure but also on the mechanical properties, in particular, the fatigue resistance of LB-PBF-processed metallic materials. The commonly used 316L SS is chosen for the experimental programme in this study because of its higher ductility and lower sensitivity to volumetric defects under cyclic loading.[23] Therefore, if there are any effects of build platform preheating on the fatigue strength of LB-PBF 316L SS, greater effects are expected for materials with less ductility and more sensitivity to volumetric defects.

2 | MATERIAL AND METHODS

The austenitic 316L SS powder (17.7Cr-0.02C-12.6Ni-0.87Mn-0.67Si-2.29Mo) was used in this study. The Renishaw AM 250 additive system, an LB-PBF method, was used to fabricate the specimens. Two sets of cylindrical bars (to be machined to fatigue specimens) and net-shaped tensile test specimens were fabricated. In order to study the effect of build platform preheating on the microstructure/defect structure and consequently mechanical performance of the material, the first set of specimens was fabricated without preheating the build platform (designated as non-preheated (NP)), whereas the build platform was preheated to 150°C (designated as P150) for fabricating the second set (150°C is the maximum temperature that could be reached with the AM machine used in this study). The same process parameters (laser power 200 W, hatching distance 0.11 mm, scan speed 1833.3 $mm.s^{-1}$ and layer thickness 0.05 mm), except the preheating temperature, were used to fabricate all the parts. It is worth noting that no heat treatment was applied to the specimens in this study. The cylindrical bars were further machined to round fatigue specimens with straight gage sections. Figure 1 presents the final geometry and dimensions for fatigue and tensile test specimens following ASEM E606[24] and ASTM E8,[25] respectively.

The effect of preheating the build platform on the microstructural features, including the melt pool, defect size and population, and grain structure, was studied in the gage section of the fabricated specimens. To perform the melt pool analysis, specimens were cross sectioned perpendicular to the final laser track on the very top layer that was not affected by a subsequent layer deposition and thus represented the nominal process condition.[26] The melt pool boundaries were further revealed on the longitudinal plane parallel to the build direction (i.e., longitudinal cross section) by chemical etching (using $HCL:HNO_3:CH_3COOH$ etchant). In order to analyse the size and distribution of the volumetric defects (i.e., gas-entrapped pores, LoF), X-ray CT scans were made using a Zeiss Xradia 620 system for 3D visualization and comparison of the porosity level in each

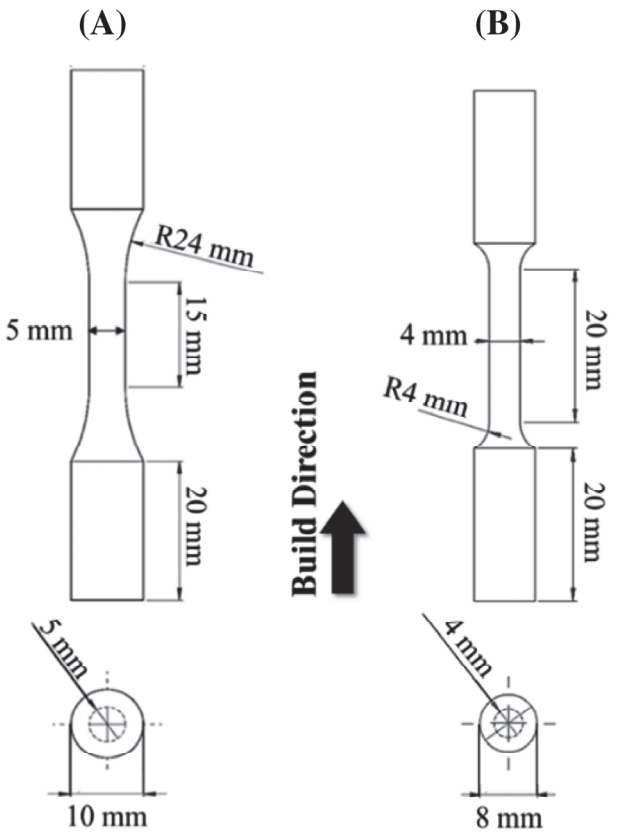

FIGURE 1 The final geometry and dimensions of (A) fatigue and (B) tensile specimens.CEM3311

condition (i.e., NP and P150). Electron backscatter diffraction (EBSD) scanning was also performed on the mirror-finished polished longitudinal cross sections using a Zeiss Crossbeam 550 scanning electron microscope (SEM)/focused ion beam (FIB) for microstructure characterization.

Quasi-static tensile and uniaxial fully reversed, strain-controlled fatigue tests were conducted using an MTS Landmark servohydraulic load frame with a 100-kN load cell. An MTS extensometer was used to measure the strains accurately during quasi-static and cyclic deformations. Tensile tests were conducted at 0.001 s^{-1} at ambient temperature in two steps: first, the test was conducted up to 0.045 $mm.mm^{-1}$ of strain with the extensometer mounted on the specimen to measure the strain. The extensometer was then removed to avoid any damage to the extensometer because of the limitation in its travel distance, and the test was continued after 0.045 mm mm^{-1} of strain in displacement-controlled mode until fracture. Two tensile tests were conducted for each condition (i.e., NP and P150) to check the repeatability of the results. Uniaxial fully reversed ($R_\varepsilon = -1$), strain-controlled fatigue tests were carried out in the range of 0.00175–0.0040 $mm.mm^{-1}$ of strain amplitudes to cover the cyclic behaviour of the material from low cycle fatigue (LCF) to high cycle fatigue (HCF) regimes. The test frequencies were attuned for each strain level to obtain a similar average cyclic strain rate of approximately 0.02 s^{-1}. Finally, fractography analysis was performed on the fracture surfaces using the SEM to shed light on the fatigue failure mechanisms.

3 | RESULTS AND DISCUSSION

In this section, the experimental observations on the microstructure/defect structure and mechanical properties of LB-PBF 316L SS are presented for the specimens fabricated in NP build platform and preheated build platform to 150°C (P150). The effects of preheating the platform on the melt pool size, defect size and distribution and crystallographic orientation of grains are inspected. The resulting mechanical properties, including tensile and fatigue, of NP and P150 LB-PBF 316L SS are presented and discussed comprehensively with respect to the differences seen in the material's microstructure/defect structure (i.e., structure–property relationships).

3.1 | Microstructure characterization

Figure 2 presents the melt pool analysis for the specimens from NP (Figure 2A) and P150 (Figure 2B) conditions on their longitudinal plane parallel to the build direction (shaded *YZ*-plane in the schematic), as shown schematically. It can be seen from this figure that the melt pools are shallower in NP condition (∼90 μm) as compared with the P150 one (∼150 μm). The melt pool depth has been reported to have an impact on the formation of volumetric defects (e.g., gas-entrapped pores and LoF).[27,28] However, it has been shown that the melt pool depth is not the only parameter to influence the formation of volumetric defects but also overlap depth can be very influential, specifically in the formation of LoF defects.[6,26] In this regard, NASA has proposed a method to conduct the melt pool analysis through normalizing the melt pool depth, d_p, and overlap depth, d_o, by the layer thickness, t_l, to evaluate the probability of formation of volumetric defects.[26] The d_p/t_l and d_o/t_l ratios for NP condition (Figure 2A) are calculated to be 1.8 and 1.3, respectively, which are lower than those of P150 condition (3 and 1.85, respectively). The higher melt pool and overlap depth ratios for the P150 condition as compared with the ones for the NP condition are associated with the effect of preheating the build platform on the thermal history experienced by the parts during fabrication. Preheating the build platform at 150°C was

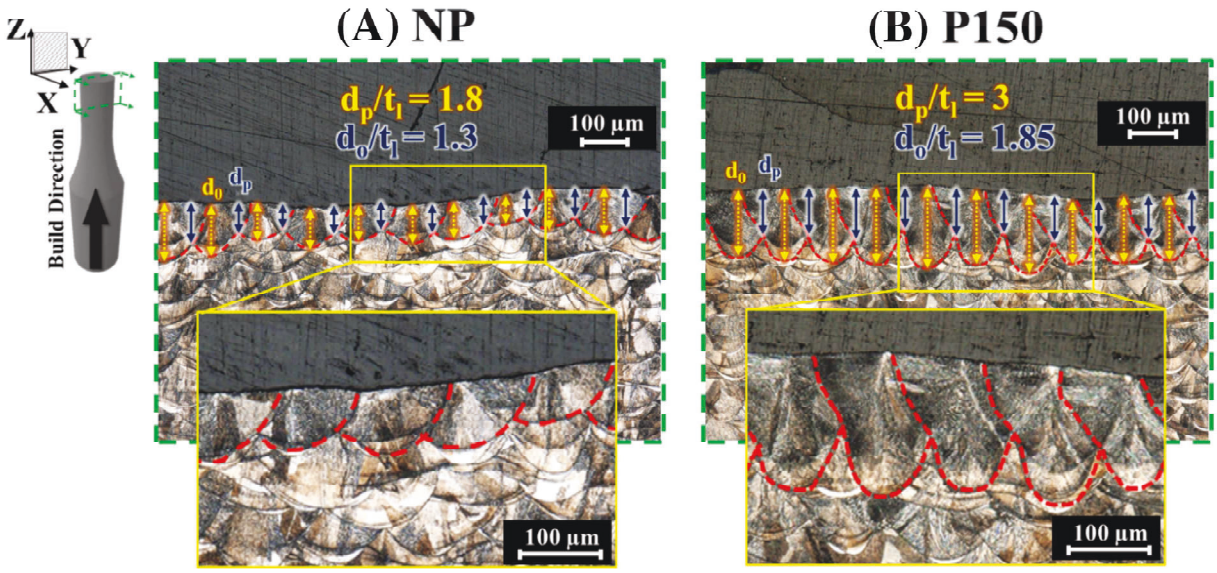

FIGURE 2 Melt pool characterization following the method proposed by NASA[26] for (A) non-preheated (NP) and (B) preheated to 150°C (P150) conditions [Colour figure can be viewed at wileyonlinelibrary.com]

simulated to reduce the cooling rate by about 14% as compared with the condition that the build platform was not preheated.[29]

The deeper melt pools in P150 condition as compared with those of NP ones may be due to the higher temperature of the previously fused layers, while a new layer is fabricated. The lower temperature difference between the previously solidified layers and the newly fabricated layer can result in a lower cooling/solidification rate. Considering the deeper melt pools and lower cooling/solidification rates for P150 condition as compared with the NP condition, it is expected for P150 specimens to have smaller/fewer pores and LoF defects than the NP ones. The low cooling/solidification rates provide more time for the gas-entrapped pores to escape from the melt pool during solidification, and the sufficient overlap depth in the P150 condition reduces the chance of LoF formation, or at least smaller LoF defects are expected to be formed.

There may be a height dependency for the effect of preheating the build platform on the part's structure. To evaluate such effects, gage sections of an NP and a P150 specimen were scanned from bottom to top, and the change in the size distribution of volumetric defects in each condition is compared visually in Figure 3. It can be seen that preheating the build platform (Figure 3B) decreases the size and population of the defects throughout the gage section as compared with the condition where the build platform is not preheated (Figure 3A). As was expected, the effect of preheating on the structure is alleviated slightly towards the top of the specimen's gage section (~40–45 mm far from the build platform); fewer and smaller defects are observed in the bottom and

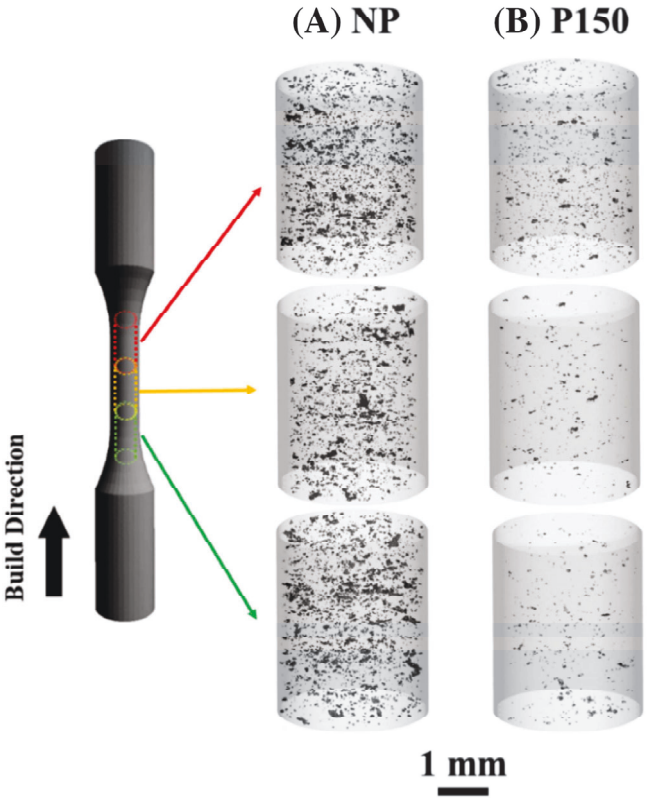

FIGURE 3 X-ray CT scan results throughout the gage section of the laser beam powder bed fused (LB-PBF) 316L stainless steel (SS) specimens from (A) non-preheated (NP) and (B) preheated to 150°C (P150) conditions [Colour figure can be viewed at wileyonlinelibrary.com]

middle of the gage section as compared with the top part. Note that the bottom part of the gage section is almost more than 25 mm far from the build platform, and still

preheating the build platform impacts the defects' size and number up to an approximate height of 45 mm from the build platform. Therefore, one should be careful with taking advantage of preheating the build platform for taller parts; however, the affected height may be increased by increasing the preheating temperature. The effect of an increased preheating temperature beyond 150°C is to be studied systematically in the future.

The X-ray CT results presented in Figure 4 show both the visual and statistical evaluation of volumetric defects in the middle of the gage section for NP and P150 specimens. Similar to the results presented in Figure 3, there are more and larger volumetric defects in NP condition (Figure 4A) as compared with the P150 one (Figure 4B); some examples of LoF defects and gas-entrapped pores are highlighted in Figure 4A,B by red and green colours, respectively. The diameter of the defects, obtained by taking the square root of the projected area of each defect on the loading plane for NP and P150 specimens, was also compared statistically in Figure 4C.

The statistical results show that the NP specimens possess more and larger volumetric defects (i.e., gas-entrapped pores and LoF defects) than the P150 ones. Note that statistics are taken from the sliced radial cross sections of the scanned volume, with these sections being apart with the distance more than the maximum height

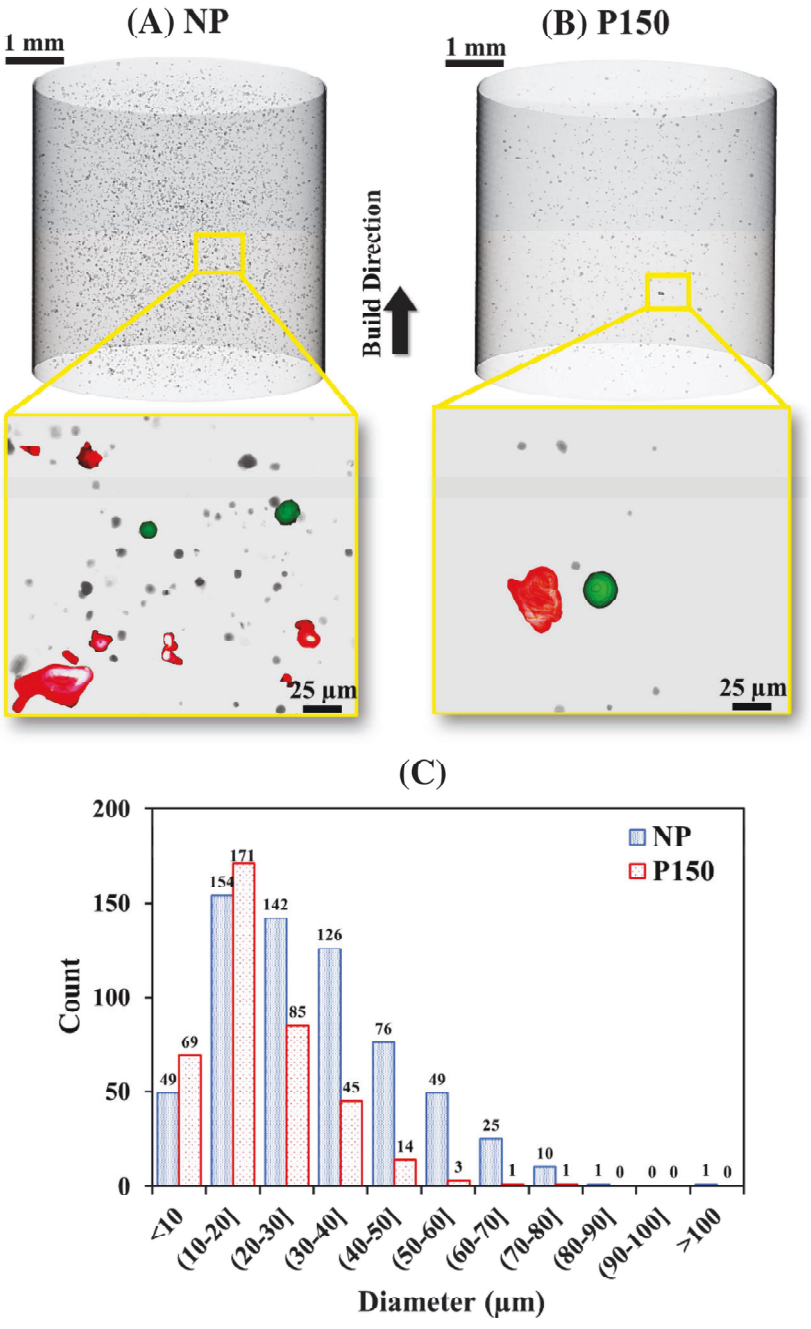

FIGURE 4 X-ray CT scan results from a small section (~5 mm) of the gage section of machined laser beam powder bed fused (LB-PBF) 316L stainless steel (SS) specimens for (A) non-preheated (NP) and (B) preheated to 150°C (P150) conditions, as well as (C) defects size distributions based on 100 radial cross-sections [Colour figure can be viewed at wileyonlinelibrary.com]

of defects to avoid duplication in the results. Therefore, the results presented in Figure 4C do not represent the entire pore size distribution, and they are just for the comparison. The largest diameter of defect in the entire scanned volume of each specimen was also detected to be 163 and 94 μm, respectively, for NP and P150 specimens. It must be noted that the size and distribution of the defects throughout the specimen may be somewhat different from these statistics as only a small section of the gage length was scanned (∼5 mm) and about 100 radial cross sections were analysed. However, the results prove that the P150 specimens contain less and smaller volumetric defects as compared with the NP specimens.

If the melt pool depths and overlap depths are sufficiently large, the previously fused layers are affected by the subsequently deposited layer; that is, the previous layers will be partially/thoroughly remelted. The d_o should be at least larger than the layer thickness, t_l, to avoid the formation of the LoF defect[26]; however, if the d_o/t_l ratio becomes close to 2, the probability of formation of LoF defects will be reduced significantly. In the case of NP condition, although the ratio of d_p/t_l and d_o/t_l is larger than 1, they are not close to 2, which increases the chance for the formation of gas-entrapped pores and LoF defects, respectively (see Figure 4A). On the other hand, in the P150 condition, although the d_p is three times larger than the t_l, resulting in fewer and smaller gas-entrapped pores (see Figure 4B), the d_o/t_l is 1.85 and smaller than 2 (note that it is still larger than d_o/t_l in NP specimens). Therefore, LoF defects are also formed in P150 condition, but they are smaller and fewer in number than those in NP specimens (see Figure 4C).

The thermal history experienced by the part can also affect the grain structure.[5] The microstructure of the LB-PBF 316L SS in NP and P150 conditions is presented in Figure 5. The inverse pole figure (IPF) maps show the microstructure in *YZ*-plane (i.e., parallel to the build direction and loading direction). As seen, similar to the other AM materials reported in the literature,[30–32] grains

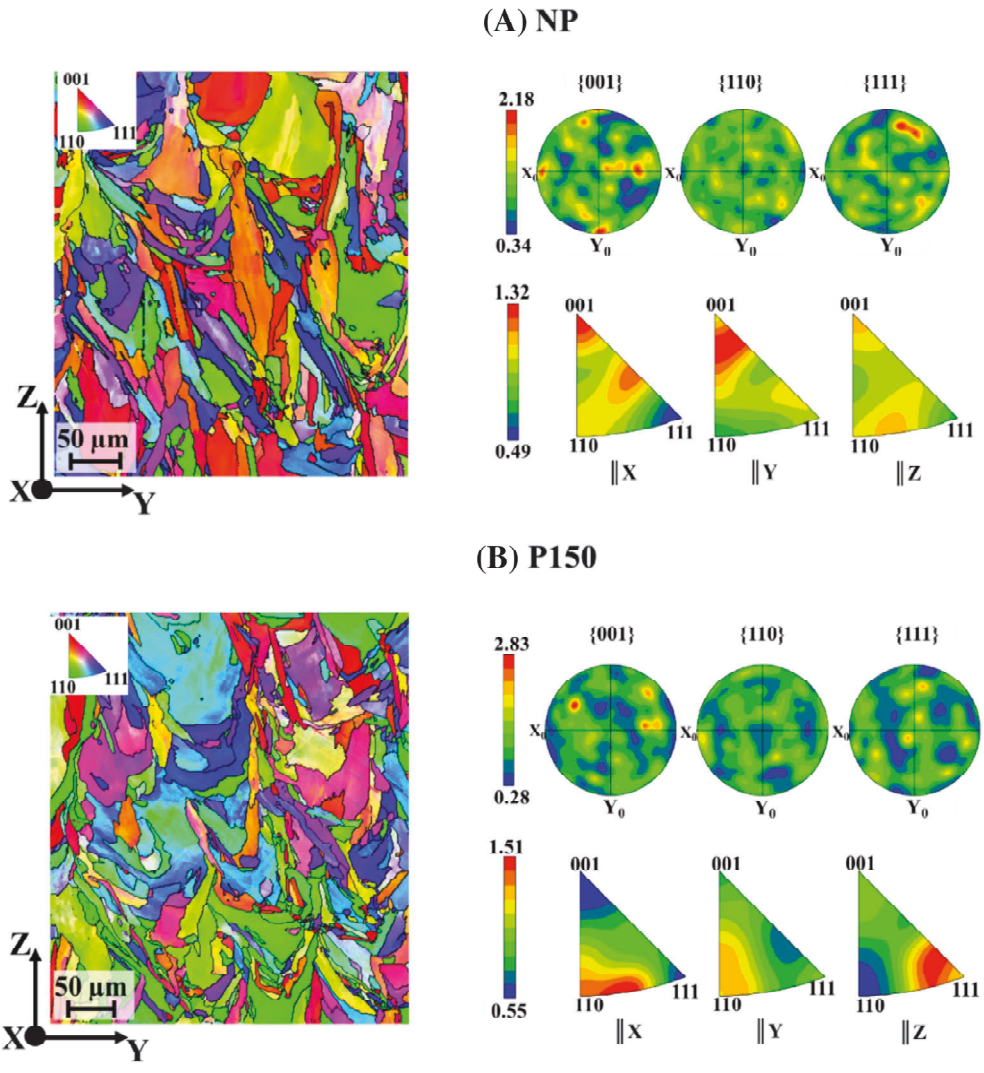

FIGURE 5 Microstructure and crystallographic characterization on the longitudinal plane; inverse pole figure (IPF) maps along the *z*-axis as well as pole figures and IPFs for (A) non-preheated (NP) and (B) preheated to 150°C (P150) specimens [Colour figure can be viewed at wileyonlinelibrary.com]

are elongated along the heat dissipation path towards the build platform. In NP condition (Figure 5A), the set of pole figures and IPFs (see //*X* and//*Y*) show that the austenite, γ, grains are mostly <001> oriented. In fact, <001> is the easy solidification growth direction for cubic structures (e.g., face-centred cubic (FCC) or body-centred cubic (BCC) structures), and grains grow epitaxially in this direction.[13]

Interestingly, preheating the build platform up to 150°C alters the crystallographic orientation of the γ grains, as seen in Figure 5B; the grain orientation is changed from <001> to <110> and <111>. This is most likely associated with the lower thermal gradient and the solidification rate in the P150 condition. It is well established that the thermal gradient along the melt pool walls during the solidification influences the grain orientation.[33,34] Sun et al.[35] reported that an increase in the heat input, resulting in lower thermal gradient and lower cooling rate, can change the grain orientation of LB-PBF 316L from <001> to <110>, similar to the results obtained for P150 condition in this study. Therefore, preheating the build platform resembles the condition where the process parameters are attuned to obtain a higher heat input for reaching a lower cooling/solidification rate during AM processes.

The well-known microstructure characteristic of the AM materials, cellular structure,[36,37] for both conditions is shown in Figure 6; however, the cells are more equiaxed and even appear to be finer in the P150 condition (see Figure 6B) as compared with the NP condition (see Figure 6A). This can be explained by the lower temperature gradient and consequently lower cooling/solidification rates for the P150 condition as compared with the NP one. Moreover, it appears that preheating the build platform may lead to recrystallization of the grains; subgrains are formed in P150 condition (shown by yellow dashed arrows/boundaries in Figure 6B); however, the subgrains could not turn into the grains with high angle boundaries and result in grain refinement (average grain size of 16 μm was calculated for both NP and P150 conditions using EBSD results). This may be explained by insufficient preheating temperature to provide adequate driving force energy for recrystallization of the grains.

3.2 | Quasi-static tensile behaviour

Reduction in the fraction of volumetric defects and the alteration in the crystallographic orientation of γ grains may impact the mechanical properties of the material.

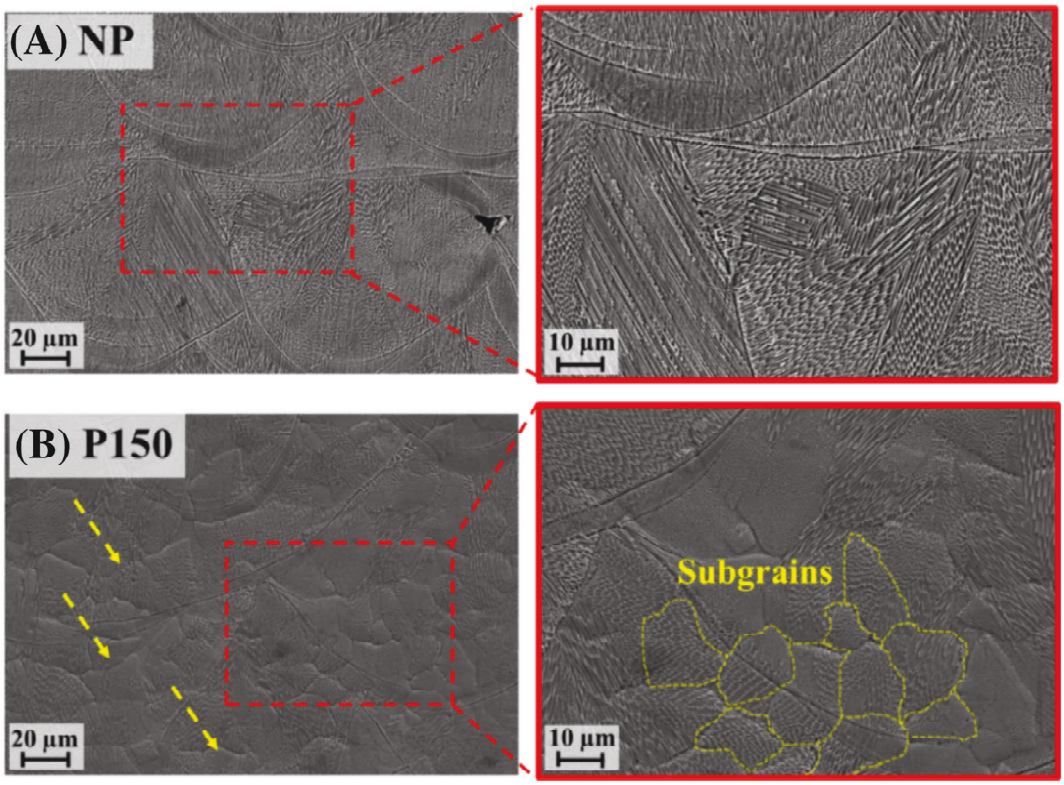

FIGURE 6 Microstructure characterization of laser beam powder bed fused (LB-PBF) 316L stainless steel (SS) (on the longitudinal plane parallel to the build direction) fabricated in (A) non-preheated (NP) and (B) preheated to 150°C (P150) conditions showing the cellular structures [Colour figure can be viewed at wileyonlinelibrary.com]

The quasi-static tensile stress–strain curves of NP and P150 LB-PBF 316L SS are presented in Figure 7. As seen, preheating the build platform (i.e., P150 condition) increased the ductility by about 18%, without jeopardizing the strength of the material. Improved ductility may be associated with both the lower volumetric defects in P150 specimens (see Figure 4), as well as the grains orienting more along the FCC preferred slip system (i.e., <110>-/<111>-oriented grains) as compared with those in NP specimens (<100>-oriented grains) seen in Figure 5.

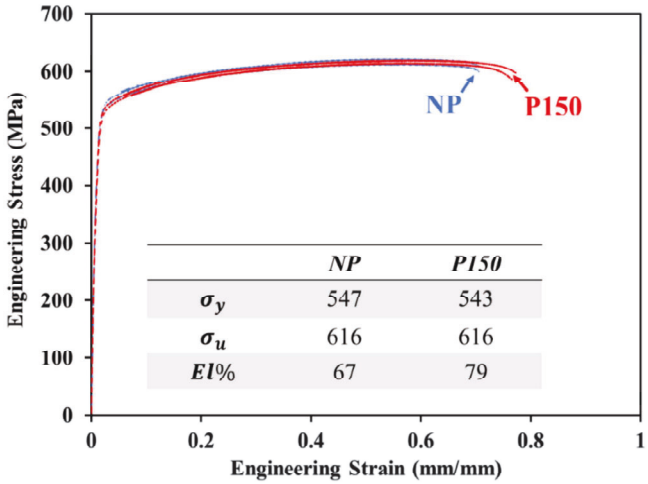

FIGURE 7 Quasi-static tensile engineering stress-engineering strain behaviour of laser beam powder bed fused (LB-PBF) 316L stainless steel (SS) fabricated in non-preheated (NP) and preheated to 150°C (P150) conditions [Colour figure can be viewed at wileyonlinelibrary.com]

The tensile fracture surfaces for both NP and P150 LB-PBF 316L SS are shown in Figure 8. In line with the X-ray CT results (see Figure 4), a higher level of volumetric defects is observed on the fracture surface of NP specimens (Figure 8A) as compared with that of the P150 counterparts (Figure 8B). Large LoF defects are characterized on the fracture surface of the NP specimen comprising unmelted powder particles, whereas there are fewer and smaller LoF defects observed for the P150 specimen Besides, a finer cellular structure can be noticed on the fracture surface of the P150 specimen in Figure 8A, as compared with the NP specimen, presented in Figure 8B.

The higher population of LoF defects in NP specimens could have contributed to the lower ductility observed. Elimination/reduction of such defects by preheating the build platform (i.e., P150 condition) assisted with the increase in the ductility under quasi-static tensile loading. In addition, grains are oriented

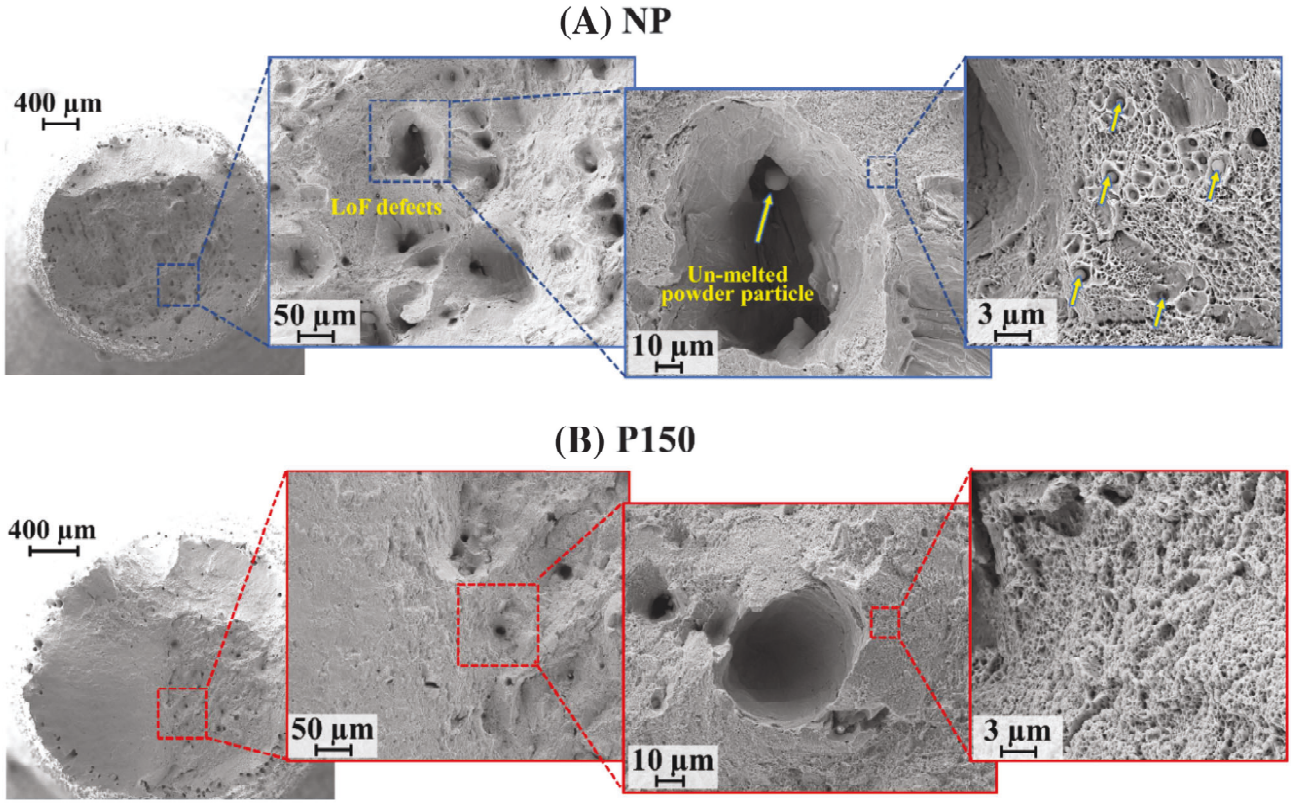

FIGURE 8 Tensile fracture surfaces of laser beam powder bed fused (LB-PBF) 316L stainless steel (SS) specimens fabricated in (A) non-preheated (NP) and (B) preheated to 150°C (P150) conditions. The unmelted powder particles found in the lack of fusion (LoF) defects are shown by yellow arrows [Colour figure can be viewed at wileyonlinelibrary.com]

along the direction of the easy slip system for FCC structure in P150 condition; thus, dislocations can cross slip and glide easier, which could have also assisted with the increased ductility and elongation in P150 specimens. Similarly, Wang et al.[33] reported an increase in ductility of LB-PBF 316L SS as a result of containing oriented grains as compared with the condition with <100>-oriented grains, whereas the yield strength remained unchanged.

3.3 | Fatigue behaviour

Preheating the build platform had no effects on the cyclic deformation as NP and P150 specimens exhibited similar cyclic deformation behaviours, initial cyclic hardening followed by cyclic softening. In addition, the stable stress–strain hysteresis loops were identical for both conditions. The fatigue test data including total strain amplitude, ε_a, elastic strain amplitude, $\frac{\Delta\varepsilon_e}{2}$, plastic strain amplitude, $\frac{\Delta\varepsilon_p}{2}$, stress amplitude, σ_a, mean stress, σ_m, and reversals to failure, $2N_f$, are listed in Table 1. Moreover, the strain-life fatigue properties (i.e., fatigue ductility coefficient, ε'_f, fatigue ductility exponent, c, fatigue strength coefficient, σ'_f, and fatigue strength exponent, b[38]) are calculated as $\varepsilon'_f = 0.5207$, $c = -0.591$, $\sigma'_f = 563.1$ MPa and $b = -0.036$ for NP and $\varepsilon'_f = 0.2752$, $c = -0.501$, $\sigma'_f = 543.7$ MPa and $b = -0.030$ for P150. Accordingly, the strain-life fatigue data and fits for NP and P150 LB-PBF 316L SS are presented in Figure 9 (all specimens in machined surface condition). It should be noted that the tests at 0.00175 mm.mm^{-1} of strain amplitude took each more than 2 weeks, and therefore, only one test for each condition was performed at this strain level. This was because of the applied test frequency ($f = 2.85$ Hz) to keep the average cyclic strain rate constant among all tests. As seen in Figure 9, there is some improvement in fatigue performance of LB-PBF 316L SS across life regimes by preheating the build platform up to 150°C, which is most likely due to the lower volumetric

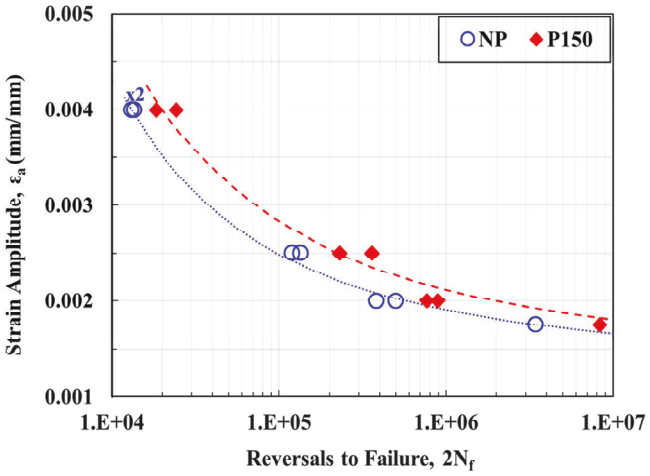

FIGURE 9 Strain-life fatigue data and fits for machined laser beam powder bed-fused (LB-PBF) 316L stainless steel (SS) specimens fabricated in non-preheated (NP) and preheated to 150°C (P150) conditions [Colour figure can be viewed at wileyonlinelibrary.com]

TABLE 1 Uniaxial fully reversed, strain-controlled fatigue test results of machined LB-PBF 316L SS fabricated in NP and P150 conditions, as well as the $\sqrt{\text{area}}$ of the crack initiating defects based on the Murakami's approach

Specimen ID	ε_a (mm.mm^{-1})	f (Hz)	$\frac{\Delta\varepsilon_e}{2}$ (mm.mm^{-1})	$\frac{\Delta\varepsilon_p}{2}$ (mm.mm^{-1})	σ_a (MPa)	σ_m (MPa)	$2N_f$ (reversals)	$\sqrt{\text{area}}$ of defect(s) (μm)
NP_1	0.00175	2.86	0.00172	0.00003	337	−32	3 446 774	264
NP_2	0.0020	2.5	0.00190	0.00010	352	−31	499 108	153, 190, 161
NP_3	0.0020	2.5	0.00190	0.00010	364	−24	384 138	144, 83, 24, 71
NP_4	0.0025	2	0.00200	0.00050	391	−22	134 976	221
NP_5	0.0025	2	0.00200	0.00050	384	−23	119 996	337
NP_6	0.0040	1.25	0.00210	0.00190	415	−9	13 630	256
NP_7	0.0040	1.25	0.00210	0.00190	415	−9	13 064	237
P150_1	0.00175	2.86	0.00172	0.00003	339	−21	8 308 714	139
P150_2	0.0020	2.5	0.00190	0.00010	360	−21	893 014	68
P150_3	0.0020	2.5	0.00190	0.00010	361	−29	765 648	191
P150_4	0.0025	2	0.00200	0.00050	382	−16	360 264	132
P150_5	0.0025	2	0.00200	0.00050	384	−28	231 006	323
P150_6	0.0040	1.25	0.00210	0.00190	418	−7	24 238	97
P150_7	0.0040	1.25	0.00210	0.00190	414	−7	18 452	191

Abbreviations: LB-PBF, laser beam powder bed fused; NP, non-preheated; P150, preheated to 150°C; SS, stainless steel.

defects, specifically LoF ones, in the P150 specimens as compared with the NP counterparts.

It is well established that the portion of overall fatigue life spent in the crack initiation stage becomes larger at the HCF regime.[38] On the other hand, the cracks often initiate from volumetric defects in AM specimens in the machined surface condition, and thus, the more the volumetric defects are present, the more chance for the cracks to initiate and propagate. Moreover, it has been shown that the larger the defects are, the shorter the fatigue lives become.[4,39,40] Accordingly, the longer fatigue lives for P150 specimens in the HCF regime are attributed to the fewer and smaller volumetric defects as compared with NP specimens (see Figure 4). Although preheating the build platform may have a marginal impact on the residual stresses in the part, it is shown that the fracture mechanism of the LB-PBF 316L SS is somewhat independent of the residual stresses.[41] In addition, residual stresses have been found to be only induced in shallow depths from the surface of a part built vertically[42,43]; therefore, the residual stresses were most likely removed as the specimens were deeply machined in this study. Accordingly, the observed improvement in the fatigue behaviour of P150 specimens can be credited to their reduced number and size of volumetric defects.

The crack initiating defect size based on the Murakami's $\sqrt{area}$ approach is reported for all the

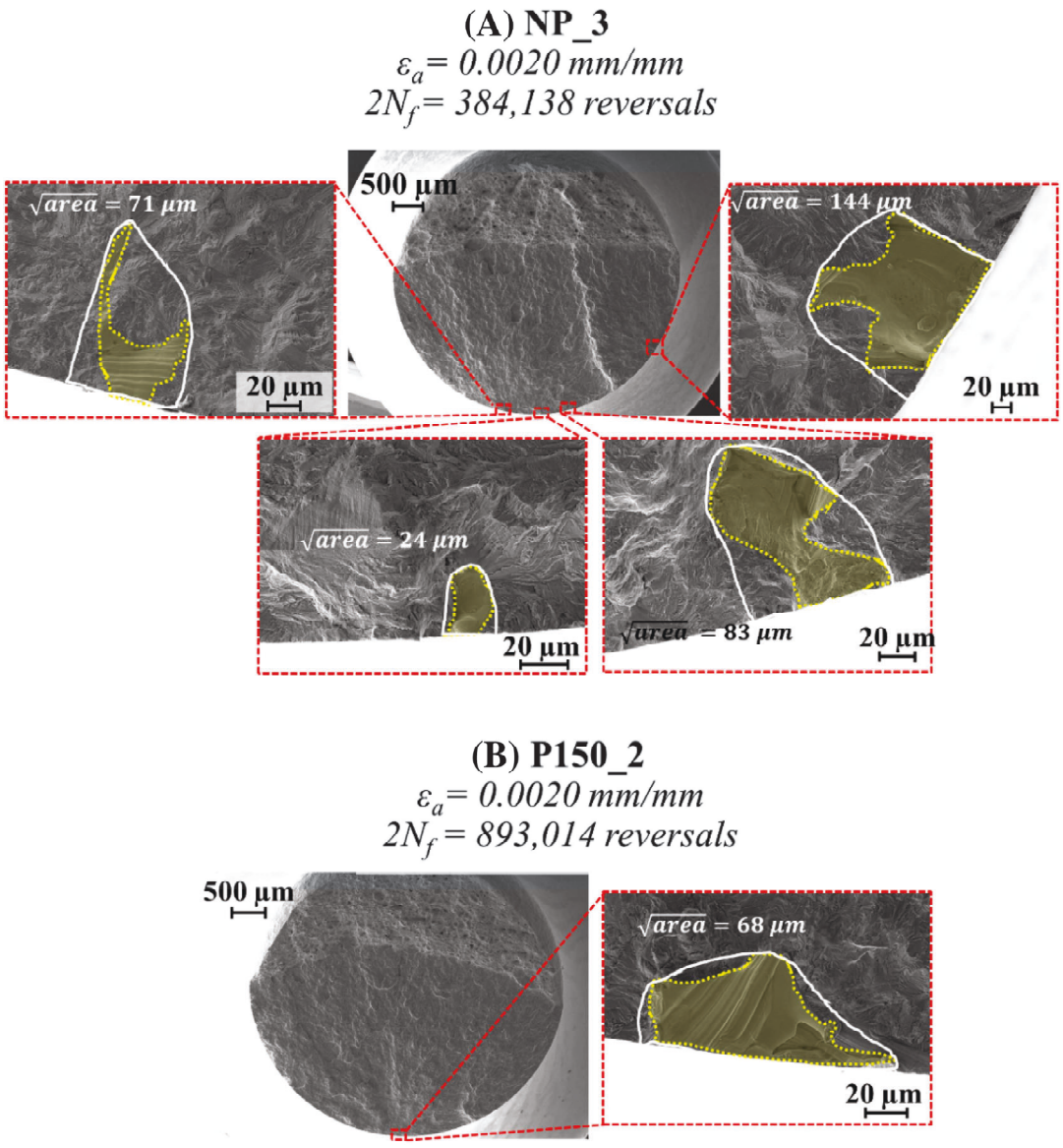

FIGURE 10 Fracture surface of the machined laser beam powder bed fused (LB-PBF) 316L stainless steel (SS) specimens in (A) non-preheated (NP) and (B) preheated to 150°C (P150) conditions and tested at 0.0020 mm.mm^{-1} of strain amplitude. Note that the defect area is filled with dashed yellow curves, whereas the defect area based on Murakami's approach is shown with solid white curves [Colour figure can be viewed at wileyonlinelibrary.com]

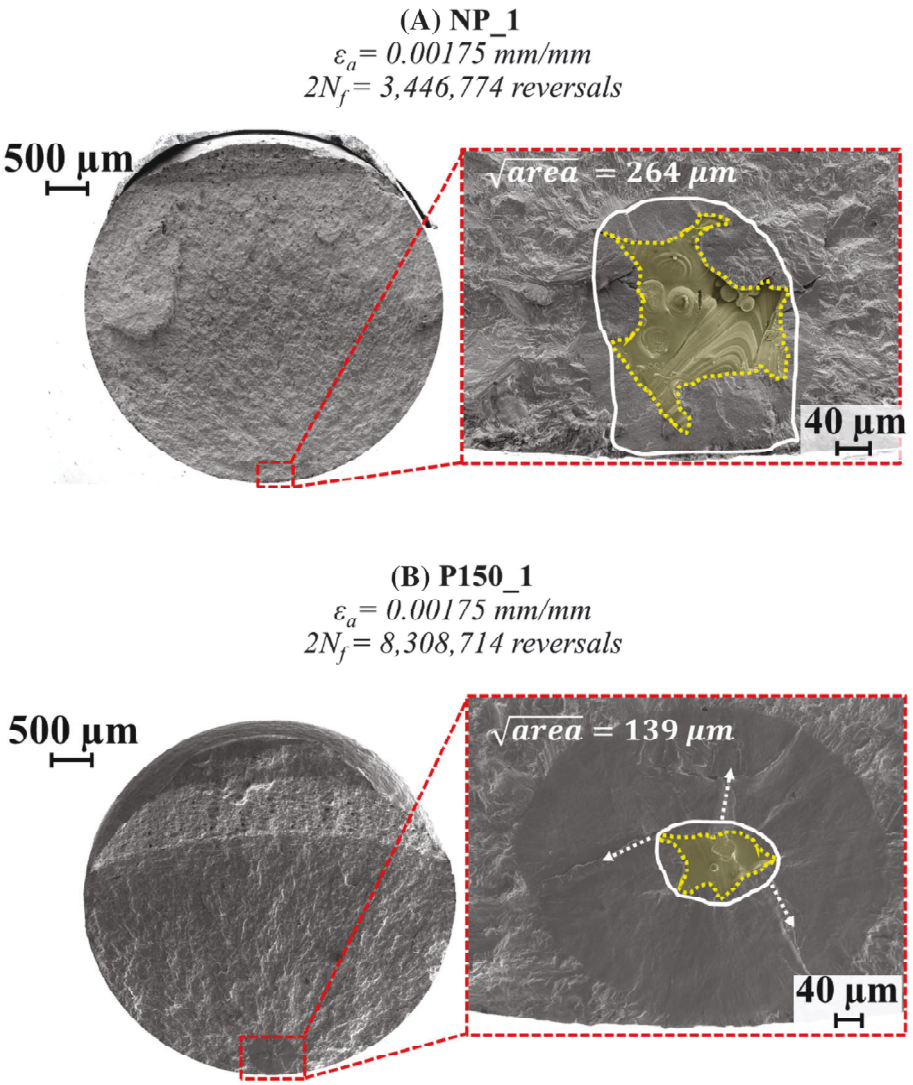

FIGURE 11 Fracture surfaces of the machined laser beam powder bed fused (LB-PBF) 316L specimens fabricated in (A) non-preheated (NP) and (B) preheated to 150°C (P150) conditions and tested at 0.00175 mm. mm^{-1} of strain amplitude. Note that the defect area is filled with dashed yellow curves, whereas the defect area based on Murakami's approach is shown with solid white curves [Colour figure can be viewed at wileyonlinelibrary.com]

specimens in Table 1.[4,44–46] Figure 10 shows the fracture surfaces of the NP and P150 specimens tested at 0.0020 mm.mm^{-1} of strain amplitude. As seen, several cracks initiated from LoF defects in both conditions. However, in NP specimen (Figure 10A), cracks started from four LoF defects close to the surface with $\sqrt{area}$ of 144, 83, 71, and 24 µm, whereas in P150 specimen (Figure 10B), cracks started from one defect with $\sqrt{area}$ of 68 µm. Preheating the build platform then can considerably assist with reducing the volumetric defects and potentially enhance the fatigue performance of AM materials. It is worth noting that the fatigue performance of 300 SS series is not much sensitive to defects and their effects are typically alleviated by the microstructure and ductility.[23] As can be seen in Figure 11A, for an NP specimen (NP_1 specimen) tested at 0.00175 mm mm^{-1} of strain amplitude, the crack initiated from a large LoF defect ($\sqrt{area}$ = 264 µm) close to the surface; however, the fatigue life is still considerably long due to the low sensitivity of this material to the defects. For the P150 LB-PBF 316L SS counterpart (P150_1 specimen) tested at the same strain amplitude level (i.e., 0.00175 mm.mm^{-1}), the fatigue life is 2.5 times longer than the NP specimen. It can be observed in Figure 11B that this is due to the fact that the crack initiated from a smaller internal LoF defect ($\sqrt{area}$ = 139 µm) as compared with the large, close to the surface LoF defect in the NP one ($\sqrt{area}$ = 165 µm). As seen, the internal defect created a fisheye failure pattern[47,48] in the P150 LB-PBF 316L SS specimen, which led to a longer fatigue life (8 308 714 reversals) as compared with the NP specimen (3 446 774 reversals) tested at the same strain amplitude.

4 | CONCLUSIONS

The effect of preheating the build platform (process) on the porosity level and microstructure (structure) as well as tensile and fatigue behaviour (property) of LB-PBF 316L SS was investigated. Specifically, the microstructure/defect structure (i.e., the volumetric defect size and distribution, grain structure and crystallographic

orientation of the grains) was correlated with the consequent mechanical properties of the material in NP and preheated build platform to 150°C (P150) conditions. The following conclusions can be drawn from the experimental results and observations:

1. Because of the reduced temperature gradient between the melt pool and the bulk solidified material, preheating the build platform lowered the cooling/solidification rates, which resulted in deeper melt pools as compared with the condition that the build platform was not preheated.
2. Fewer and smaller volumetric defects (i.e., gas-entrapped pores and LoF) were formed by preheating the build platform because of the higher melt pool and overlap depths in P150 condition. However, the beneficial effect of preheating seemed to be dependent on the height of the part.
3. The crystallographic orientation of grains was changed from <100> to <110> and <111> by preheating the build platform because of variation in thermal history experienced during fabrication. In addition, finer and more equiaxed cellular structures were formed in P150 condition as compared with the NP one, which contained more needle-like dendritic cellular structure.
4. Subgrains were formed in the microstructure of the P150 specimens; however, because of the insufficient preheating temperature, recrystallization did not occur to form finer grains.
5. Total elongation to failure of P150 LB-PBF 316L SS under quasi-static tensile loading was enhanced by about 18% as compared with the NP counterpart, which was attributed to the fewer and smaller defects, the finer cellular structure and the grain orientation along with the preferred FCC slip system in the P150 condition.
6. Preheating the build platform enhanced the fatigue resistance of LB-PBF 316L SS reasonably well in all the life regimes investigated in this study. This improvement was explained by the presence of fewer and smaller volumetric defects in the preheated condition as compared with the condition when the build platform was not preheated.

ACKNOWLEDGEMENT

This material is based upon the work partially supported by the U.S. Naval Air Systems Command (NAVAIR).

DATA AVAILABILITY STATEMENT

The data that support the findings of this study are available from the corresponding author upon reasonable request.

DISCLAIMER

N. S. is one of the Guest Editors of this Special Issue on Fatigue and Fracture of Additively Manufactured Materials in the *Fatigue & Fracture of Engineering Materials & Structures (FFEMS)*. The editorial and peer-review process for this article was handled by the journal's Editor-in-Chief, Prof. Youshi Hong. Furthermore, the authors of this article do not have access to any confidential information related to its peer-review process.

NOMENCLATURE

b	fatigue strength exponent
c	fatigue ductility exponent
f	frequency
N_f, $2N_f$	cycles to failure, reversals to failure
R_ε	ratio of minimum to maximum strain
γ	austenite
σ_a	stress amplitude
σ'_f	fatigue strength coefficient
σ_m	mean stress
σ_y	yield strength
σ_u	ultimate tensile strength
ε_{max}	maximum strain
ε_{min}	minimum strain
ε_a	total strain amplitude
ε'_f	fatigue ductility coefficient
$\frac{\Delta\varepsilon_p}{2}$	plastic strain amplitude
$\frac{\Delta\varepsilon_e}{2}$	elastic strain amplitude

ABBREVIATIONS

AM	additive manufacturing/additively manufactured
BCC	body-centred cubic
EB-PBF	electron beam powder bed fused
EBSD	electron backscatter diffraction
El%	percent elongation to failure
FCC	face-centred cubic
FIB	focused ion beam
HCF	high cycle fatigue
IPF	inverse pole figure
LB-PBF	laser beam powder bed fusion/fused
LCF	low cycle fatigue
LoF	lack of fusion
NP	non-preheated
P150	preheated to 150°C
SEM	scanning electron microscope/microscopy
SS	stainless steel

ORCID

Nima Shamsaei https://orcid.org/0000-0003-0325-7314

REFERENCES

1. Rafi HK, Starr TL, Stucker BE. A comparison of the tensile, fatigue, and fracture behavior of Ti–6Al–4V and 15-5 PH stainless steel parts made by selective laser melting. *Int J Adv Manuf Technol*. 2013;69:1299-1309.
2. Yadollahi A, Shamsaei N. Additive manufacturing of fatigue resistant materials: challenges and opportunities. *Int J Fatigue*. 2017;98:14-31.
3. Russell R, Wells D, Waller J, et al. Qualification and certification of metal additive manufactured hardware for aerospace applications. In: *Additive Manufacturing for the Aerospace Industry*. Elsevier; 2019:33-66.
4. Solberg K, Berto F. What is going on with fatigue of additively manufactured metals? *Mater Des Process Commun*. 2019;1-4.
5. Shamsaei N, Yadollahi A, Bian L, Thompson SM. An overview of direct laser deposition for additive manufacturing; part II: mechanical behavior, process parameter optimization and control. *Addit Manuf*. 2015;8:12-35.
6. Tang M, Pistorius PC, Beuth JL. Prediction of lack-of-fusion porosity for powder bed fusion. *Addit Manuf*. 2017;14:39-48.
7. Cunningham R, Narra SP, Montgomery C, Beuth J, Rollett AD. Synchrotron-based X-ray microtomography characterization of the effect of processing variables on porosity formation in laser power-bed additive manufacturing of Ti-6Al-4V. *Jom*. 2017;69:479-484.
8. Shrestha R, Nezhadfar PD, Masoomi M, Simsiriwong J, Pham N, Shamsaei N. Effects of design parameters on thermal history and mechanical behavior of additively manufactured 17-4 PH stainless steel. *Proceedings of the 29th Annual International Solid Freeform Fabrication Symposium—An Additive Manufacturing Conference*. 2018;1277-1289.
9. Shrestha R, Shamsaei N, Seifi M, Phan N. An investigation into specimen property to part performance relationships for laser beam powder bed fusion additive manufacturing. *Addit Manuf*. 2019;29:1-14.
10. Yadollahi A, Shamsaei N, Thompson SM, Seely DW. Effects of process time interval and heat treatment on the mechanical and microstructural properties of direct laser deposited 316L stainless steel. *Mater Sci Eng a*. 2015;644:171-183.
11. Nezhadfar PD, Anderson-Wedge K, Daniewicz SR, Phan N, Shao S, Shamsaei N. Improved high cycle fatigue performance of additively manufactured 17-4 PH stainless steel via in-process refining micro-/defect-structure. *Addit Manuf*. 2020;36:1-15.
12. Averyanova M, Cicala E, Bertrand P, Grevey D. Experimental design approach to optimize selective laser melting of martensitic 17-4 PH powder: part I—single laser tracks and first layer. *Rapid Prototyp J*. 2012;18:28-37.
13. DebRoy T, Wei HL, Zuback JS, et al. Additive manufacturing of metallic components—process, structure and properties. *Prog Mater Sci*. 2018;92:112-224.
14. Daniewicz SR, Shamsaei N. An introduction to the fatigue and fracture behavior of additive manufactured parts. *Int J Fatigue*. 2017;94:167.
15. Gockel J, Sheridan L, Koerper B, Whip B. The influence of additive manufacturing processing parameters on surface roughness and fatigue life. *Int J Fatigue*. 2019;124:380-388.
16. Aboulkhair NT, Everitt NM, Ashcroft I, Tuck C. Reducing porosity in AlSi10Mg parts processed by selective laser melting. *Addit Manuf*. 2014;1:77-86.
17. Beuth J, Fox J, Gockel J, et al. Process mapping for qualification across multiple direct metal additive manufacturing processes
18. Mertens R, Vrancken B, Holmstock N, Kinds Y, Kruth JPP, Van Humbeeck J. Influence of powder bed preheating on microstructure and mechanical properties of H13 tool steel SLM parts. *Phys Procedia*. 2016;83:882-890.
19. Yang KV, Shi Y, Palm F, Wu X, Rometsch P. Columnar to equiaxed transition in Al-Mg(-Sc)-Zr alloys produced by selective laser melting. *Scr Mater*. 2018;145:113-117.
20. Raghavan N, Dehoff R, Pannala S, et al. Numerical modeling of heat-transfer and the influence of process parameters on tailoring the grain morphology of IN718 in electron beam additive manufacturing. *Acta Mater*. 2016;112:303-314.
21. Li W, Liu J, Zhou Y, et al. Effect of substrate preheating on the texture, phase and nanohardness of a Ti–45Al–2Cr–5Nb alloy processed by selective laser melting. *Scr Mater*. 2016;118:13-18.
22. Leung CLA, Tosi R, Muzangaza E, Nonni S, Withers PJ, Lee PD. Effect of preheating on the thermal, microstructural and mechanical properties of selective electron beam melted Ti-6Al-4V components. *Mater Des*. 2019;174:1-10.
23. Pegues JW, Roach MD, Shamsaei N. Additive manufacturing of fatigue resistant austenitic stainless steels by understanding process-structure–property relationships. *Mater Res Lett*. 2020;8:8-15.
24. ASTM International. *E606/E606M-12 Standard Test Method for Strain-Controlled Fatigue Testing*. West Conshohocken, PA: ASTM International; 2012. https://doi.org/10.1520/E0606_E0606M-12
25. ASTM E8. Standard test methods for tension testing of metallic materials. 2006;i: 1–24.
26. NASA. MSFC-SPEC-3717—specification for control and qualification of laser powder bed fusion metallurgical processes. 2017: 58.
27. Narra SP. Melt pool geometry and microstructure control across alloys in metal based additive manufacturing processes. Carnegie Mellon University. Thesis; 2018. https://doi.org/10.1184/R1/6720569.v1
28. Scime L, Beuth J. Melt pool geometry and morphology variability for the Inconel 718 alloy in a laser powder bed fusion additive manufacturing process. *Addit Manuf*. 2019;29:1-9.
29. Nezhadfar PD, Soltani-Tehrani A, Shamsaei N. Effect of preheating build platform on microstructure and mechanical properties of additively manufactured 316L stainless steel. *Proceedings of the 30th Annual International Solid Freeform Fabrication Symposium—An Additive Manufacturing Conference*. 2019;415-425.
30. Nezhadfar PD, Shrestha R, Phan N, Shamsaei N. Fatigue behavior of additively manufactured 17-4 PH stainless steel: synergistic effects of surface roughness and heat treatment. *Int J Fatigue*. 2019;124:188-204.
31. Tucho WM, Cuvillier P, Sjolyst-Kverneland A, Hansen V. Microstructure and hardness studies of Inconel 718 manufactured by selective laser melting before and after solution heat treatment. *Mater Sci Eng a*. 2017;689:220-232.

32. Pegues J, Roach M, Williamson RS, Shamsaei N. Surface roughness effects on the fatigue strength of additively manufactured Ti-6Al-4V. *Int J Fatigue*. 2018;116:543-552.
33. Wang X, Muñiz-Lerma JA, Attarian Shandiz M, Sanchez-Mata O, Brochu M. Crystallographic-orientation-dependent tensile behaviours of stainless steel 316L fabricated by laser powder bed fusion. *Mater Sci Eng a*. 2019;766:1-16.
34. Wang X, Muñiz-Lerma JA, Sánchez-Mata O, Attarian Shandiz M, Brochu M. Microstructure and mechanical properties of stainless steel 316L vertical struts manufactured by laser powder bed fusion process. *Mater Sci Eng a*. 2018;736:27-40.
35. Sun S-H, Ishimoto T, Hagihara K, Tsutsumi Y, Hanawa T, Nakano T. Excellent mechanical and corrosion properties of austenitic stainless steel with a unique crystallographic lamellar microstructure via selective laser melting. *Scr Mater*. 2019;159:89-93.
36. Qiu C, Kindi MAL, Aladawi AS, Hatmi IAL. A comprehensive study on microstructure and tensile behaviour of a selectively laser melted stainless steel. *Sci Rep*. 2018;8(1):1-16.
37. Yin YJ, Sun JQ, Guo J, Kan XF, Yang DC. Mechanism of high yield strength and yield ratio of 316L stainless steel by additive manufacturing. *Mater Sci Eng a*. 2019;744:773-777.
38. Stephens RI, Fatemi A, Stephens RR, Fuchs HO. *Metal Fatigue in Engineering*. John Wiley & Sons; 2000.
39. Bagherifard S, Beretta N, Monti S, Riccio M, Bandini M, Guagliano M. On the fatigue strength enhancement of additive manufactured AlSi10Mg parts by mechanical and thermal post-processing. *Mater Des*. 2018;145:28-41.
40. Sterling AJ, Torries B, Shamsaei N, Thompson SM, Seely DW. Fatigue behavior and failure mechanisms of direct laser deposited Ti–6Al–4V. *Mater Sci Eng a*. 2016;655:100-112.
41. Riemer A, Leuders S, Thöne M, Richard HA, Tröster T, Niendorf T. On the fatigue crack growth behavior in 316L stainless steel manufactured by selective laser melting. *Eng Fract Mech*. 2014;120:15-25.
42. Morettini G, Razavi SMJ, Zucca G. Effects of build orientation on fatigue behavior of Ti-6Al-4V as-built specimens produced by direct metal laser sintering. *Procedia Struct Integr*. 2019;24:349-359.
43. Salmi A, Piscopo G, Atzeni E, Minetola P, Iuliano L. On the effect of part orientation on stress distribution in AlSi10Mg specimens fabricated by laser powder bed fusion (L-PBF). *Procedia CIRP*. 2018;67:191-196.
44. du Plessis A, Beretta S. Killer notches: the effect of as-built surface roughness on fatigue failure in AlSi10Mg produced by laser powder bed fusion. *Addit Manuf*. 2020;35:1-15.
45. Murakami Y. *Metal Fatigue: Effects of Small Defects and Nonmetallic Inclusions*. Elsevier; 2002.
46. Yamashita Y, Murakami T, Mihara R, Okada M, Murakami Y. Defect analysis and fatigue design basis for Ni-based superalloy 718 manufactured by selective laser melting. *Int J Fatigue*. 2018;117:485-495.
47. Schönbauer BM, Stanzl-Tschegg SE, Perlega A, et al. The influence of corrosion pits on the fatigue life of 17-4PH steam turbine blade steel. *Eng Fract Mech*. 2015;147:158-175.
48. Kawagoishi N, Chen Q, Nisitani H. Fatigue strength of Inconel 718 at elevated temperatures. *Fatigue Fract Eng Mater Struct*. 2000;23(3):209-216.

How to cite this article: Nezhadfar PD, Shamsaei N, Phan N. Enhancing ductility and fatigue strength of additively manufactured metallic materials by preheating the build platform. *Fatigue Fract Eng Mater Struct*. 2021;44:257–270. https://doi.org/10.1111/ffe.13372